

# Supersonic Impact Response of Polymer Thin Films via Large-Scale Atomistic Simulations

Andrew L. Bowman,\* Edwin P. Chan, William B. Lawrimore, and John K. Newman

Cite This: *Nano Lett.* 2021, 21, 5991–5997

Read Online

ACCESS |

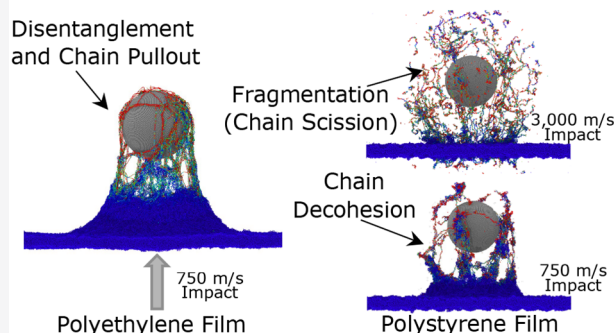
Metrics & More

Article Recommendations

Supporting Information

**ABSTRACT:** Recent nanoscale ballistic tests have shown the applicability of nanomaterials for ballistic protection but have raised questions regarding the nanoscale structure–property relationships that contribute to the ballistic response. Herein, we report on multimillion-atom reactive molecular dynamics simulations of the supersonic impact, penetration, and failure of polyethylene (PE) and polystyrene (PS) ultrathin films. The simulated specific penetration energy ( $E_p^*$ ) versus impact velocity predicts to within 15% the experimentally determined  $E_p^*$  for PS. For impact velocities less than  $1 \text{ km s}^{-1}$ , a crazing/petalling failure mode is observed due to chain disentanglement, transitioning to fragmentation coupled with large amounts of adiabatic heating at velocities greater than  $1 \text{ km s}^{-1}$ . Interestingly, the high entanglement density of PE provides enhanced penetration resistance at low velocities, whereas increased adiabatic heating in PS promotes greater penetration resistance at elevated velocities. By understanding nanoscale mechanisms of energy absorption, nanomaterials can be designed to provide superior penetration resistance.

**KEYWORDS:** Molecular Dynamics, Energy Absorption, LIPIT, Ballistic Impact, Adiabatic Heating, Thin Film



The structure–property relationships of high-velocity impacts of polymers are highly complex due to strain rate sensitivity, length-scale dependence, pressure and temperature sensitivity, and complex morphologies. Polymers have been well investigated for ballistic application due to their ability to absorb large amounts of energy at high strain rates<sup>1,2</sup> and the potential for reuse due to their self-healing properties.<sup>3</sup> Polymers also exhibit size-scale dependent properties, and ultrathin polymer films have been observed to have one of the highest specific penetration energies ( $E_p^*$ ) recorded to date.<sup>2</sup> However, the nanoscale understanding of the driving mechanisms behind the high impact resistance of polymers is not well understood.

As material systems approach the nanoscale, the structure–property relationships are not well-known. Nanoscale materials exhibit size-dependent behaviors that vary from their macro-scale counterparts. Nanoscale experiments have proven difficult to conduct, and in situ observation of nanoscale dissipation mechanisms is difficult or impossible, resulting in a large knowledge gap. This gap in understanding is compounded during ballistic and blast scenarios as shock waves travel through the material at high strain rates and pressures, possibly inducing phase transitions (e.g., glass transition, melting, etc.), disassociating bonds, and catastrophically damaging the material. Development and unification of novel experiments and simulation techniques to address these

knowledge gaps and enhance ballistic-resistant materials is a goal of this work.

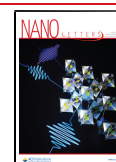
Microparticle ballistic testing via Laser-Induced Particle Impact Testing (LIPIT) has shed light on the perforation and fracture behavior of many different types of materials subjected to high-velocity impacts.<sup>4–12</sup> For thermoplastic polymers, the impact response has been well studied in PS<sup>8,9</sup> and polycarbonate (PC).<sup>10,11</sup> Entanglement density ( $\rho_e$ ) was found to enhance the  $E_p^*$  in both PS<sup>9</sup> and PC<sup>11</sup> systems, with PC exhibiting an overall higher  $E_p^*$  due to a larger  $\rho_e$ . However, the molecular mechanisms (i.e., chain scission, disentanglement, chain friction, etc.) that lead to the dominance of one energy absorption mechanism over the other are still unknown.

MD simulations of high-velocity impacts on carbon-based materials are rather limited, but a few fundamental works exist, mostly involving impacts on graphene sheets<sup>13–17</sup> or polymer thin films.<sup>18–20</sup> For example, the ballistic penetration was studied for poly(methyl methacrylate) (PMMA) to

Received: March 10, 2021

Revised: May 14, 2021

Published: July 15, 2021



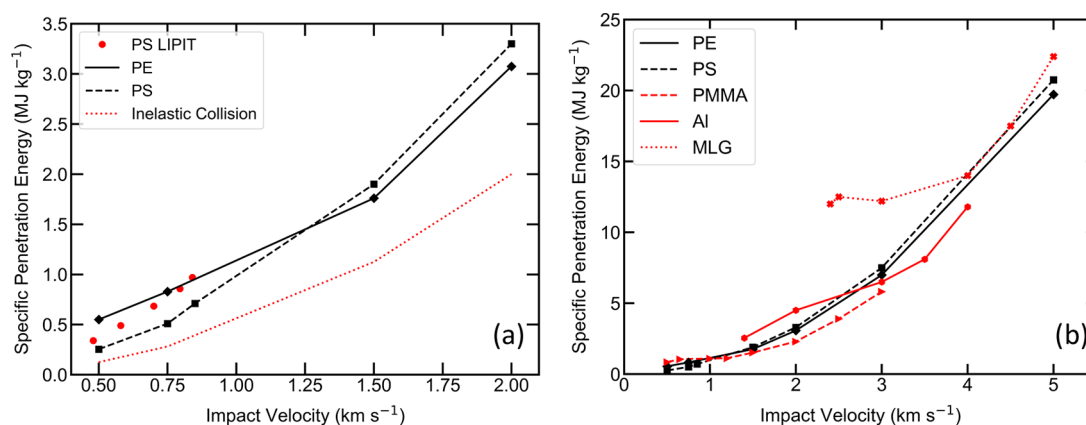


**Figure 1.** Specific ballistic penetration energy ( $E_p^*$ ) versus the projectile impact velocity ( $V_i$ ) for amorphous PE and PS systems each with chain lengths of 1000 carbon atoms (500 repeat units). (a) Comparison of the simulated results to a baseline inelastic collision and to LIPIT experiments<sup>9</sup> (red circles) on a PS thin film with a similar molecular weight. (b) Comparisons of the  $E_p^*$  versus the  $V_i$  for PE and PS compared with MD simulations<sup>19</sup> of PMMA, Al, and MLG.

compare  $E_p^*$  and local failure mechanisms of polymers, graphene, and metals.<sup>19</sup> However, bond scission was not accounted for in PMMA. Additionally, the effect of geometrical factors of the films (cross-sectional area, thickness) and projectile (diameter) was studied and shows that above the ballistic limit,  $E_p^*$  scales as expected with the projectile diameter. However, near the ballistic limit, the  $E_p^*$  scales with the projectile circumference as tearing occurs along the projectile rim. With further advances of the LIPIT technique, MD simulations are expected to be a valuable tool to answer foundational questions regarding energy absorption, particularly in materials under shock.

In this study, large-scale simulations via reactive MD are used to study the physically based molecular mechanisms involved in the penetration and failure of amorphous PE and PS thin films during supersonic (0.5 to 1.5 km s<sup>-1</sup>) and hypersonic (2–5 km s<sup>-1</sup>) impacts. Fully atomistic systems consisting of several million atoms allow for the enhanced description of frictional forces between chains that are critical in capturing stresses involved in chain pullout. The use of the Adaptive Intermolecular Reactive Bond Order (AIREBO<sup>21</sup>) potential captures the dynamic scission of bonds along the polymer backbone, distinguishing between failure via chain pullout and chain scission. Due to the large-scale (relative to typical MD scales) nature of the simulations and the small-scale and high-rate (relative to typical ballistic experiments) nature of LIPIT, the incommensurability in length- and time-scales typically observed between experiments and MD is highly reduced to produce a first-of-its-kind comparison between the two methods. In fact, identical impact velocities and similar size-scales, with a model film thickness of  $\sim 6$  nm compared to a minimum film thickness of  $\sim 60$  nm for LIPIT, are compared between the two methods. Simulations of this magnitude come with considerable cost, mainly computational resources (processors) and time. The set of simulations presented herein, each consisting of approximately 9 million atoms and 1440 processors (2.3 GHz), utilized a total computation time of over 1.2 million central processing unit (CPU) hours.

Thin films of PE and PS are constructed, equilibrated, and impacted in a complex series of simulations, totaling over 20 ns of simulation time. Interactions between the projectile (30 nm diameter) and films are described by a 12–6 Lennard-Jones

potential. Carbon–carbon and carbon–hydrogen interactions are described by the AIREBO potential. Complete details of the simulations are discussed in the [Supporting Information](#), along with a brief comparison of other atomistic potentials (i.e., Modified Embedded Atom Method [MEAM]<sup>22</sup>). The Large-scale Atomic/Molecular Massively Parallel Simulator (LAMMPS)<sup>23</sup> was used for all simulations. PS and PE thin films with molecular masses ( $M_n$ ) of 52.1 kg mol<sup>-1</sup> and 14 kg mol<sup>-1</sup> (chain backbones consisting of 1000 carbon atoms), respectively, were simulated, and the dispersity was not considered in this work. The polymer types and molecular weights were chosen to provide a comparison between structurally different systems. Because PE lacks bulky side groups, the monomeric friction coefficient (MFC) is several orders of magnitude less than PS ( $4.15 \times 10^{-13}$  vs.  $1.56 \times 10^{-8}$  Ns m<sup>-1</sup>).<sup>24</sup> Additionally, PS has a lower  $\rho_e$  due to its low molecular weight and large entanglement length (see [Figure 5](#)). Thus, comparison is made between a highly entangled system with weak entanglements (PE) and a highly viscous system with few entanglements (PS). Complete analysis of the film cross section (density, density distribution, Voronoi volume, thickness, and entanglement density) is discussed in the [Supporting Information](#).

The films described above were then subjected to a range of high-velocity impacts (0.5 to 5 km s<sup>-1</sup>) at 300 K, and the absorbed energy, fracture response, and thermal histories were recorded. Identified from previous works, the glass transition temperatures ( $T_g$ ) for PE and PS are approximately 255 K<sup>25</sup> and 370 K,<sup>26</sup> respectively. Thus, at impact, PE is in a rubbery phase while PS is in the glassy phase. All the films studied here were constructed with a target thickness of 6 nm. The  $E_p^*$  versus projectile impact velocity ( $V_i$ ) is depicted in [Figure 1a](#). For a baseline comparison, the  $E_p^*$  for an idealized inelastic collision (momentum conservation) is also plotted.  $E_p^*$  is defined as the loss of kinetic energy (KE) of the projectile normalized by the mass of the film contained within the projectile impact area and is used to compare dissimilar materials. Interestingly, at  $V_i$  below 1 km s<sup>-1</sup>, PE exhibits a higher capacity to absorb energy compared to PS, nearly twice as much. At higher impact velocities ( $>1$  km s<sup>-1</sup>), PS begins to exhibit higher energy absorption, suggesting different molecular mechanisms of energy dissipation for the two polymers in each velocity regime.

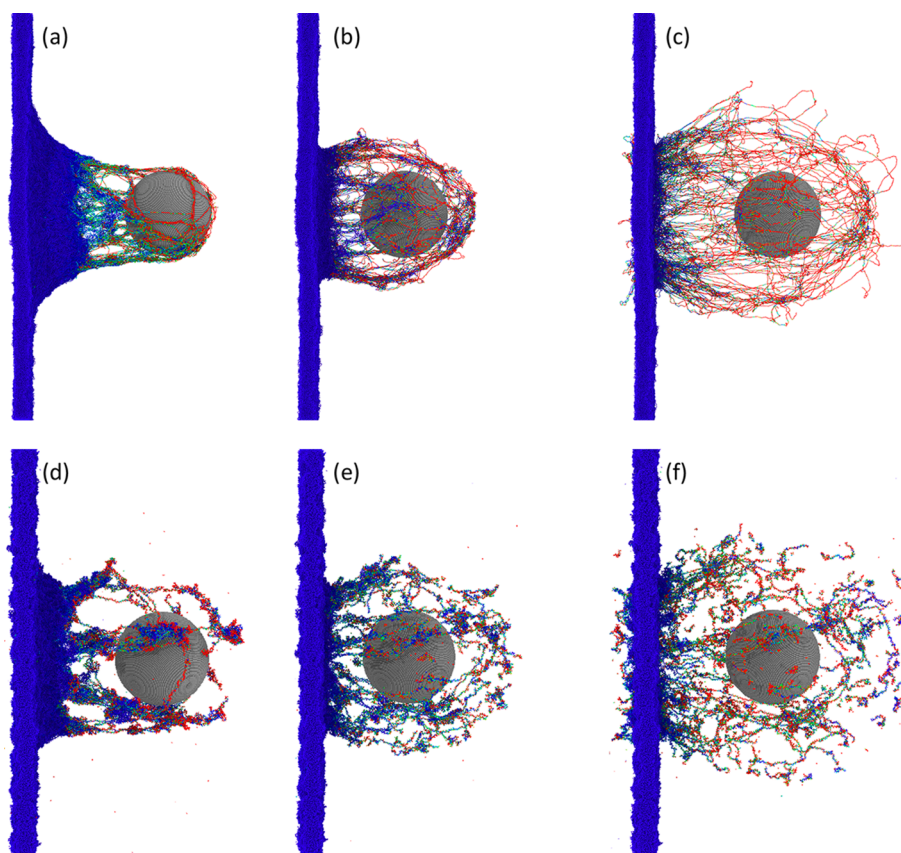


**Figure 2.** Snapshots of the ballistic failure modes for amorphous polyethylene impacted at (a)  $0.75 \text{ km s}^{-1}$ , (b)  $1.5 \text{ km s}^{-1}$ , and (c)  $3 \text{ km s}^{-1}$  and amorphous PS impacted at (d)  $0.75 \text{ km s}^{-1}$ , (e)  $1.5 \text{ km s}^{-1}$ , and (f)  $3 \text{ km s}^{-1}$ . At increased velocity, the failure mechanisms change from disentanglement (PE) and decohesion (PS) to fragmentation. Atoms are colored by volumetric atomic strain.

Figure 1a also compares the simulated and experimentally determined (via LIPIT)<sup>9</sup>  $E_p^*$  for PS with similar molecular masses ( $52.1$  vs  $51 \text{ kg mol}^{-1}$ ). Remarkably, the simulations predict the experimentally determined  $E_p^*$  to within an average error of 15%. The simulated increase of the  $E_p^*$  versus  $V_i$  curves follow similar trends observed in the experiments but slightly underpredict the simulated  $E_p^*$ . This suggests that the simulations are capturing the correct physical mechanisms during penetration but underpredict the magnitude of energy absorption. Several factors could explain the observed discrepancy: First, while the impact velocities are identical, due to the smaller diameter projectile used for the simulations, the total KE of the projectile is less than that of the experiments. While velocity (strain rate effects) dominates the thin film response, a change in total KE by scaling only the projectile mass would affect the overall inertial response of the thin film. This could explain why the slopes of the two curves are similar but shifted along the  $y$ -axis. Additionally, the projectile diameter is very close to the craze diameter, possibly limiting the formation of mature crazes. Second, the simulated thin films are about 10 times thinner than experiments, which could induce free surface and confinement effects such as chain alignment near the surface. Considering these factors, our results compare favorably and highlight the use of such simulations as a predictive design tool for ballistic resistant materials.

The impact response expanding into the hypervelocity regime, along with a comparison to other materials, is illustrated in Figure 1b. Both films display the capacity to

absorb a remarkable amount of energy due to a high strain rate dependency. The  $E_p^*$  is compared with MD simulations<sup>19</sup> of aluminum (Al), multilayered graphene (MLG), and PMMA and shows that PS and PE can approach the energy absorption capacity of pristine MLG at impact speeds greater than  $4 \text{ km s}^{-1}$ .

Figure 2 illustrates the failure modes for PE and PS impacted at low ( $0.75 \text{ km s}^{-1}$ ), intermediate ( $1.5 \text{ km s}^{-1}$ ), and high ( $3 \text{ km s}^{-1}$ ) velocity. The reader is also referred to the Supporting Information for additional atomic snapshots at different velocities and time frames. Most notably, the failure response changes from a crazing/petalling at low  $V_i$  to a fragmentation-like failure at high  $V_i$ . At low  $V_i$ , a cone-like shape is observed bending around the projectile and is especially noticeable in PE (Figure 2a). In PE, widespread chain disentanglement and void formation are clearly seen as chains are stretched and pulled from entanglement clusters. Notably, bond scission is not observed, as confirmed by other MD simulations of PE.<sup>25</sup> Due to the lack of bulky side groups in PE, the MFC is small, and chain stress remains below the maximum tensile strength, causing preferred disentanglement. The slow pullout of chains allows for more film bending, spreading the impact duration over a longer time period and larger distance, resulting in the higher values of  $E_p^*$  for PE at low  $V_i$ .

For the fracture of PS at low  $V_i$  (Figure 2d), the cone-like shape is still visible but to a lesser extent. However, a more brittle-like failure occurs via interchain decohesion. Petalling has been observed in brittle materials such as PS and graphite.<sup>5</sup> The PS simulated here has an entanglement density 3 orders of

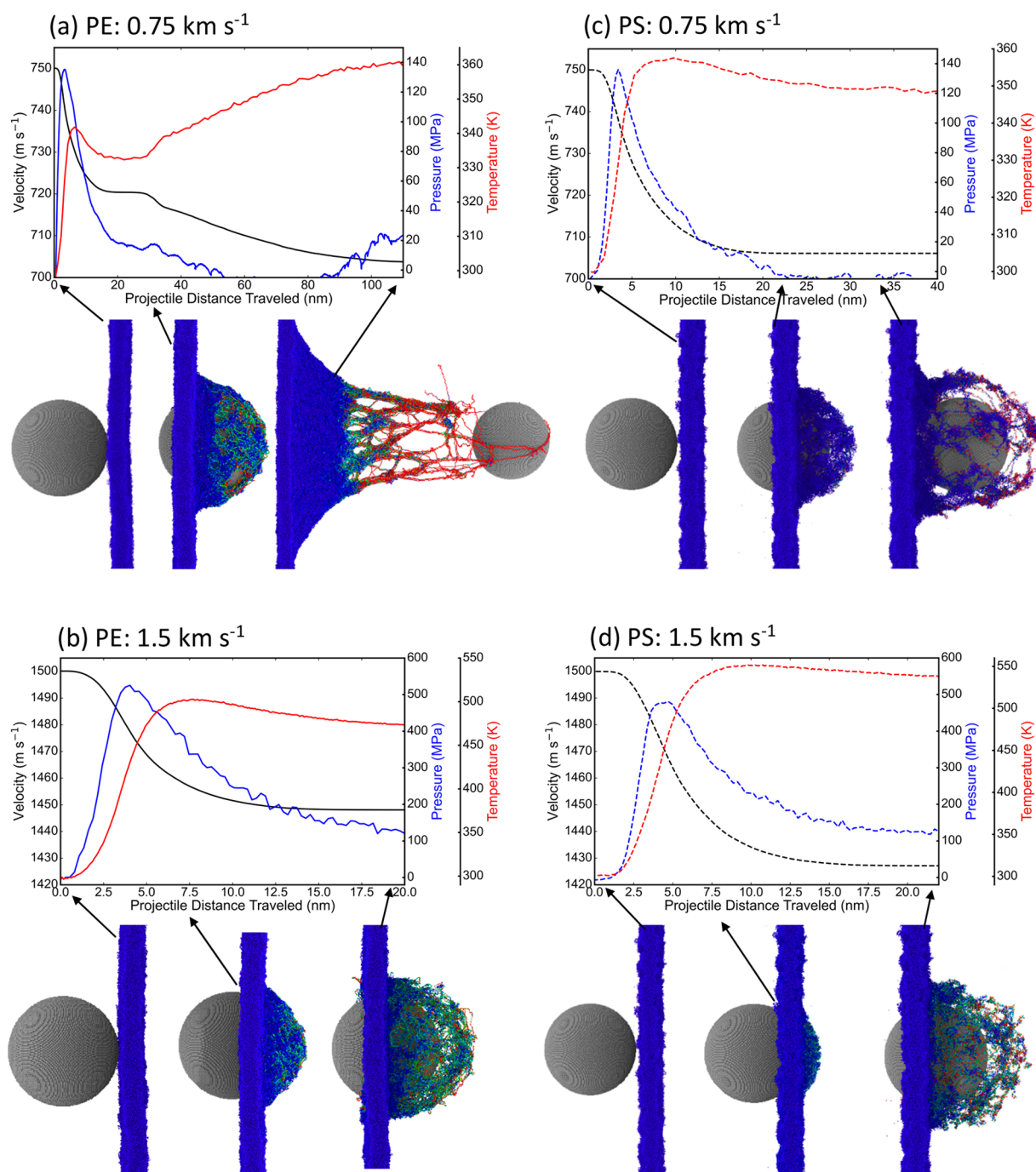


**Figure 3.** Evolution of projectile velocity, film hydrostatic pressure, and film temperature for PE (a and b) and PS (c and d) during penetration for an initial impact velocity of 750 m s<sup>-1</sup> (top row) and 1500 m s<sup>-1</sup> (bottom row). Snapshots of penetration are shown to illustrate the location of the projectile at certain points.

magnitude less than the simulated PE (Figure 5) resulting in a lack of craze formation and an inability to sustain large amounts of chain stretching. Thus, the impact duration is much shorter compared to PE. Again, bond scission is not observed at low  $V_i$  for PS.

Figure 2b,c and e,f depict the failure modes for PE and PS at a  $V_i$  of 1.5 and 3 km s<sup>-1</sup>, respectively. A similar fragmentation-like failure is observed for the two polymers at higher velocities, with impact-face debris evident and a large back-face fragmentation cloud visible. Minimal chain scission is observed in PE, while PS experiences bond scission at higher  $V_i$  ( $\approx 10$  at 3 km s<sup>-1</sup>). In PS, ductility is increased as the temperature rises

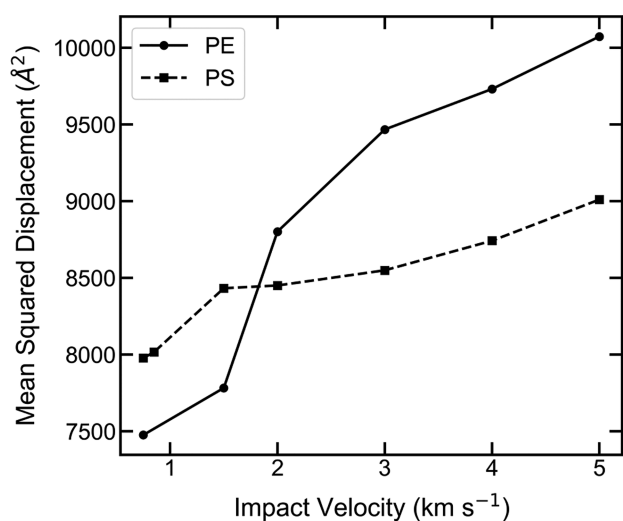
above the  $T_g$ , and some chain pullout is observed, but due to a large MFC, the interchain frictional forces within some entanglement clusters are higher than the tensile strength of the carbon backbone, causing chains to rupture. Although rupture of individual bonds does not dissipate high amounts of energy (see SI Figure S4), bond rupture promotes chain mobility as the tension in highly stressed chains is relieved along the backbone. Impact simulations by Giuntoli et al.<sup>20</sup> confirm that bond energy has a small direct role in the total energy dissipation and interchain frictional forces dominate.

Figure 3 depicts the evolution of the projectile velocity, film pressure, and film temperature as a function of the position of

the projectile for a low ( $0.75 \text{ km s}^{-1}$ ) and intermediate ( $1.5 \text{ km s}^{-1}$ ) velocity impact for PE and PS. Temperature degradation is not captured well by the AIREBO potential (see Figure S6); hence, the temperature and pressure analysis herein focuses on the supersonic impact regime before temperature degradation occurs. Indicated in Figure 3a and c, for  $V_i = 0.75 \text{ km s}^{-1}$ , the temperature begins to slowly rise as the projectile first contacts the thin film, and a shock wave passes through the material causing a rapid spike in hydrostatic pressure. The pressure spike quickly dissipates as the projectile perforates the film, while adiabatic heating continues through chain friction, and the projectile's speed is reduced. This phenomenon matches very closely to the description of the dissipation process in LIPIT experiments for PS.<sup>8</sup> Once the projectile has traveled completely through the film ( $\approx 30 \text{ nm}$ ), the resulting curves for PS and PE deviate as PE chains can undergo additional pullout before the projectile completely perforates the film (Figure 2a). Note, the pressure and temperature histories shown in Figure 3a are not accurate once the polymer chains begin to stretch and crazing occurs (penetration distance  $>30 \text{ nm}$ ) as the deformation is highly localized.

As the  $V_i$  increases, the maximum temperatures increase (Figure 3b and d). Through adiabatic heating attributed to a large MFC,<sup>24</sup> PS reaches temperatures greater than PE, which causes PS to transition into the rubbery phase. The maximum temperature achieved for each  $V_i$  is given in Figure S5 and shows that the point at which the PS transitions above  $T_g$  occurs at  $\sim 1 \text{ km s}^{-1}$ . This implies that chain mobility increases and influences the energy dissipation and failure modes of PS, confirming the assertion that PS is highly influenced by adiabatic heating due to the increase in ductility via the transition from the glassy state to the rubbery state.<sup>8,9</sup>

To quantify chain mobility, the mean squared displacement (MSD) within the impact region is plotted versus  $V_i$  in Figure 4. Since the MFC and  $\rho_e$  are different between the two polymers, the raw values of MSD are not a good metric to compare the relaxation processes of the two polymers; however, MSD is a good metric to illustrate enhanced chain mobility in response to different impact conditions. Notably, the MSD for both polymers increases with increasing  $V_i$  (and  $E_p^*$ ), indicating a connection between chain mobility and



**Figure 4.** Mean squared displacement versus impact velocity within the impact region for PE and PS.

toughness that has been recently observed experimentally.<sup>27,28</sup> Due to a high  $\rho_e$ , PE initially has a low MSD that continuously increases with  $V_i$ . PS has an initial increase in MSD up to  $1.5 \text{ km s}^{-1}$ , after which an elbow in the data is observed and the MSD increases at a slower rate, suggesting that as the temperature increases with increasing  $V_i$ , the MFC is reduced and chain mobility is enhanced. The increase in chain mobility observed in PS allows for a more ductile failure, which increases the energy absorption capacity over PE at elevated  $V_i$ .

An important factor to address is the pressure achieved during impact. Phase transitions are connected to the density of the polymer and have been shown to shift with increasing pressure<sup>29</sup> by the constraint of local and relative motion of molecules, which can act to increase the yield point, shift the  $T_g$ , and prompt a more brittle-like failure. Shift of the degradation temperature has also been observed,<sup>30</sup> especially in PS and PE as the evaporation rate of degradation products is decreased at elevated pressure. Therefore, a highly complex relationship exists between pressure, temperature, phase transitions, and chain dynamics during ballistic impacts. For the highest  $V_i$  simulated in this work ( $5 \text{ km s}^{-1}$ ), the maximum pressures observed were 4.6 and 4.05 GPa for PE and PS, respectively. These pressures are quite significant; however, since the films are not confined, the spikes in pressure are short and quickly dissipate. Comparatively lower pressures ( $\sim 150 \text{ MPa}$ ), which have less effect on chain dynamics, are achieved at impact velocities of  $0.75 \text{ km s}^{-1}$ ,

Finally, to investigate the dependence on entanglements, the  $E_p^*$  is plotted versus the  $\rho_e$  for PE and PS along with experimental LIPIT results for PS<sup>9</sup> and PC<sup>11</sup> at similar impact velocities ( $\sim 800 \text{ m s}^{-1}$ ). In order to provide a direct comparison of  $\rho_e$ , the  $\rho_e$  is estimated from the molecular weight ( $M_n$ ) and entanglement length ( $M_e$ ) in the same fashion as other experimental works,<sup>9,11</sup> based on the model of Bersted.<sup>31</sup> For simulations, this method requires topological algorithms,<sup>32–35</sup> discussed in the Supporting Information, to determine the entanglement length. Figure 5 shows that the simulated  $E_p^*$  for PS follows closely with the LIPIT results at

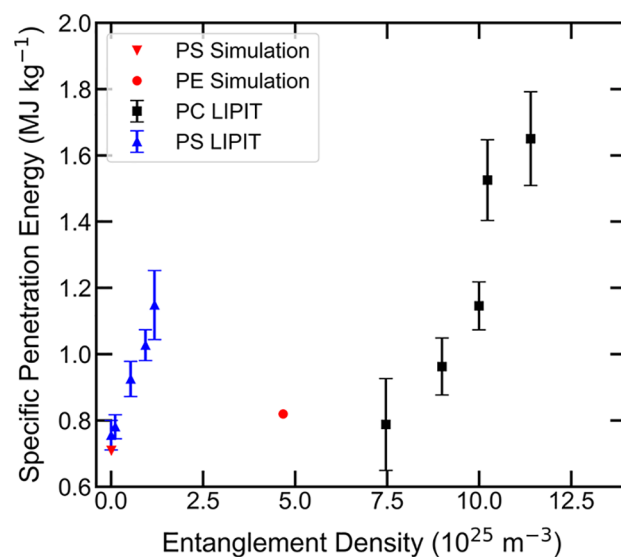


**Figure 5.** Specific penetration energy versus entanglement density for simulated impacts on PS and PE thin films compared to LIPIT experiments of PC<sup>11</sup> and PS.<sup>9</sup> The uncertainties represent one standard deviation in measured values.

low  $\rho_e$ . Overall, it is evident that  $E_p^*$  increases with increasing  $\rho_e$ . The  $E_p^*$  for PE lies between PS and PC and requires a more detailed analysis of the effects of  $M_e$  and entanglements. The low  $M_e$  for PC results in a high  $\rho_e$ , corresponding to the highest  $E_p^*$  values. Conversely, low  $M_e$  PS results in the lowest  $E_p^*$  due to an extremely low  $\rho_e$ . There appears to be a molecular structure-related dependence on the  $E_p^*$  versus  $\rho_e$  correlation, as the results for PS and PC have similar slopes (assuming linearity) but are shifted along the  $x$ -axis ( $\rho_e$  axis). This likely indicates different interchain forces that influence the amount of energy dissipation during perforation and suggests that  $E_p^*$  is not only related to the  $\rho_e$  but also depends on the friction coefficient related to interchain forces. This relationship is expected to be nonlinear and highly rate sensitive and is the subject of current ongoing work.

To conclude, ballistic impacts of PE and PS thin films are studied via large-scale MD simulations to investigate the dissipated energy, deformation and fracture response, and temperature and pressure evolutions during impact. Several factors were validated against LIPIT experiments, including  $E_p^*$ , entanglement influence, and fracture behavior. Entanglement density, MFC, and chain mobility were shown to be influential factors on the ballistic behavior but require further investigation to establish the complex relationships. Adiabatic heating induces large temperature rises during impact, especially in PS, causing PS to transition into the rubbery phase, enhancing chain mobility. PE exhibited no bond scission during impact and deformed via mechanisms of chain pullout (via  $\rho_e$  and MFC). On the other hand, PS exhibited increasing bond scission with increasing impact velocity (high MFC), possibly contributing to greater  $E_p^*$  values at elevated impact speeds. At hypervelocity, a regime not yet achievable via LIPIT, large magnitudes of  $E_p^*$  were observed for both PE and PS rivalling that of MLG. In combination with experiments, these simulations provide insights into the underlying molecular failure mechanisms associated with nanoscale ballistic impacts and provide a useful simulation tool for the design and development of impact resistance nanomaterials.

## ■ ASSOCIATED CONTENT

### SI Supporting Information

The Supporting Information is available free of charge at <https://pubs.acs.org/doi/10.1021/acs.nanolett.1c00961>.

Details of the simulation setup and methodology, postprocessing details, comparison of AIREBO and MEAM potentials, and additional atomistic snapshots of impacts (PDF)

## ■ AUTHOR INFORMATION

### Corresponding Author

**Andrew L. Bowman** – *Engineer Research and Development Center, Vicksburg, Mississippi 39180, United States of America*; [orcid.org/0000-0002-9399-3325](https://orcid.org/0000-0002-9399-3325); Phone: 662-769-7231; Email: [andrew.l.bowman@usace.army.mil](mailto:andrew.l.bowman@usace.army.mil)

### Authors

**Edwin P. Chan** – *Materials Science and Engineering Division, National Institute of Standards and Technology, Gaithersburg, Maryland 20899, United States of America*; [orcid.org/0000-0003-4832-6299](https://orcid.org/0000-0003-4832-6299)

**William B. Lawrimore** – *Engineer Research and Development Center, Vicksburg, Mississippi 39180, United States of America*

**John K. Newman** – *Engineer Research and Development Center, Vicksburg, Mississippi 39180, United States of America*

Complete contact information is available at: <https://pubs.acs.org/10.1021/acs.nanolett.1c00961>

### Notes

The authors declare no competing financial interest.

## ■ ACKNOWLEDGMENTS

The work presented by the authors was supported by the U.S. Army Engineer Research and Development Center (ERDC). Permission to publish was granted by the Director, Geotechnical and Structures Laboratory. Certain commercial equipment, instruments, or materials are identified in this paper in order to specify the experimental procedure adequately. Such identification is not intended to imply recommendation or endorsement by the National Institute of Standards and Technology, nor is it intended to imply that the materials or equipment identified are necessarily the best available for the purpose.

## ■ REFERENCES

- (1) Omar, M. F.; Akil, H. M.; Ahmad, Z. A. Measurement and Prediction of Compressive Properties of Polymers at High Strain Rate Loading. *Mater. Eng.* **2011**, *32* (8), 4207–4215.
- (2) Cai, J.; Thevamaran, R. Superior Energy Dissipation by Ultrathin Semicrystalline Polymer Films Under Supersonic Microprojectile Impacts. *Nano Lett.* **2020**, *20* (8), 5632–5638.
- (3) Wool, R. P. Self-Healing Materials: A Review. *Soft Matter* **2008**, *4* (3), 400–418.
- (4) Xie, W.; Alizadeh-Dehkharghani, A.; Chen, Q.; Champagne, V. K.; Wang, X.; Nardi, A. T.; Kooi, S.; Müftü, S.; Lee, J.-H. Dynamics and Extreme Plasticity of Metallic Microparticles in Supersonic Collisions. *Sci. Rep.* **2017**, *7* (1), 5073.
- (5) Lee, J.-H.; Loya, P. E.; Lou, J.; Thomas, E. L. Dynamic Mechanical Behavior of Multilayer Graphene via Supersonic Projectile Penetration. *Science* **2014**, *346* (6213), 1092–1096.
- (6) Veysset, D.; Hsieh, A. J.; Kooi, S. E.; Nelson, K. A. Molecular Influence in High-Strain-Rate Microparticle Impact Response of Poly(Urethane Urea) Elastomers. *Polymer* **2017**, *123*, 30–38.
- (7) Veysset, D.; Hsieh, A. J.; Kooi, S.; Maznev, A. A.; Masser, K. A.; Nelson, K. A. Dynamics of Supersonic Microparticle Impact on Elastomers Revealed by Real-Time Multi-Frame Imaging. *Sci. Rep.* **2016**, *6* (1), 25577.
- (8) Hyon, J.; Lawal, O.; Fried, O.; Thevamaran, R.; Yazdi, S.; Zhou, M.; Veysset, D.; Kooi, S. E.; Jiao, Y.; Hsiao, M.-S.; Streit, J.; Vaia, R. A.; Thomas, E. L. Extreme Energy Absorption in Glassy Polymer Thin Films by Supersonic Micro-Projectile Impact. *Mater. Today* **2018**, *21* (8), 817–824.
- (9) Xie, W.; Lee, J.-H. Dynamics of Entangled Networks in Ultrafast Perforation of Polystyrene Nanomembranes. *Macromolecules* **2020**, *53* (5), 1701–1705.
- (10) Chen, S. H.; Souna, A. J.; Soles, C. L.; Stranick, S. J.; Chan, E. P. Using Microprojectiles to Study the Ballistic Limit of Polymer Thin Films. *Soft Matter* **2020**, *16* (16), 3886–3890.
- (11) Chan, E. P.; Xie, W.; Orski, S. V.; Lee, J.-H.; Soles, C. L. Entanglement Density-Dependent Energy Absorption of Polycarbonate Films via Supersonic Fracture. *ACS Macro Lett.* **2019**, *8* (7), 806–811.
- (12) Lee, J.-H.; Veysset, D.; Singer, J. P.; Retsch, M.; Saini, G.; Pezeril, T.; Nelson, K. A.; Thomas, E. L. High Strain Rate

Deformation of Layered Nanocomposites. *Nat. Commun.* **2012**, *3* (1), 1164.

(13) Meng, Z.; Han, J.; Qin, X.; Zhang, Y.; Balogun, O.; Keten, S. Spalling-like Failure by Cylindrical Projectiles Deteriorates the Ballistic Performance of Multi-Layer Graphene Plates. *Carbon* **2018**, *126*, 611–619.

(14) Meng, Z.; Singh, A.; Qin, X.; Keten, S. Reduced Ballistic Limit Velocity of Graphene Membranes Due to Cone Wave Reflection. *Extreme Mech. Lett.* **2017**, *15*, 70–77.

(15) Azevedo, D. L.; Bizao, R. A.; Galvao, D. S. Molecular Dynamics Simulations of Ballistic Penetration of Penta-Graphene Sheets. *MRS Adv.* **2018**, *3* (8–9), 433–437.

(16) Wang, S.; Gao, E.; Xu, Z. Interfacial Failure Boosts Mechanical Energy Dissipation in Carbon Nanotube Films under Ballistic Impact. *Carbon* **2019**, *146*, 139–146.

(17) Xia, K.; Zhan, H.; Hu, D.; Gu, Y. Failure Mechanism of Monolayer Graphene under Hypervelocity Impact of Spherical Projectile. *Sci. Rep.* **2016**, *6* (1), 33139.

(18) Dewapriya, M. A. N.; Meguid, S. A. Comprehensive Molecular Dynamics Studies of the Ballistic Resistance of Multilayer Graphene-Polymer Composite. *Comput. Mater. Sci.* **2019**, *170*, 109171.

(19) Meng, Z.; Keten, S. Unraveling the Effect of Material Properties and Geometrical Factors on Ballistic Penetration Energy of Nanoscale Thin Films. *J. Appl. Mech.* **2018**, *85* (12), 121004.

(20) Giuntoli, A.; Hansoge, N. K.; Keten, S. Star Topology Increases Ballistic Resistance in Thin Polymer Films. *Extreme Mech. Lett.* **2020**, *41*, 101038.

(21) Brenner, D. W.; Shenderova, O. A.; Harrison, J. A.; Stuart, S. J.; Ni, B.; Sinnott, S. B. A Second-Generation Reactive Empirical Bond Order (REBO) Potential Energy Expression for Hydrocarbons. *J. Phys.: Condens. Matter* **2002**, *14* (4), 783–802.

(22) Mun, S.; Bowman, A. L.; Nouranian, S.; Gwaltney, S. R.; Baskes, M. I.; Horstemeyer, M. F. Interatomic Potential for Hydrocarbons on the Basis of the Modified Embedded-Atom Method with Bond Order (MEAM-BO). *J. Phys. Chem. A* **2017**, *121* (7), 1502–1524.

(23) Plimpton, S. Fast Parallel Algorithms for Short-Range Molecular Dynamics. *J. Comput. Phys.* **1995**, *117*, 1–19.

(24) van Meerveld, J. A Method to Extract the Monomer Friction Coefficient from the Linear Viscoelastic Behavior of Linear, Entangled Polymer Melts. *Rheol. Acta* **2004**, *43* (6), 615–623.

(25) Bowman, A. L.; Mun, S.; Nouranian, S.; Huddleston, B. D.; Gwaltney, S. R.; Baskes, M. I.; Horstemeyer, M. F. Free Volume and Internal Structural Evolution during Creep in Model Amorphous Polyethylene by Molecular Dynamics Simulations. *Polymer* **2019**, *170*, 85–100.

(26) Sharp, J. S.; Forrest, J. A. Free Surfaces Cause Reductions in the Glass Transition Temperature of Thin Polystyrene Films. *Phys. Rev. Lett.* **2003**, *91* (23), 235701.

(27) Soles, C. L.; Burns, A. B.; Ito, K.; Chan, E.; Liu, J.; Yee, A. F.; Tyagi, M. S. Importance of Sub-Nanosecond Fluctuations on the Toughness of Polycarbonate Glasses. *Macromolecules* **2020**, *53* (15), 6672–6681.

(28) Soles, C. L.; Burns, A. B.; Ito, K.; Chan, E. P.; Douglas, J. F.; Wu, J.; Yee, A. F.; Shih, Y.-T.; Huang, L.; Dimeo, R. M.; Tyagi, M. Why Enhanced Subnanosecond Relaxations Are Important for Toughness in Polymer Glasses. *Macromolecules* **2021**, *54* (5), 2518–2528.

(29) Pionteck, J. Determination of Pressure Dependence of Polymer Phase Transitions by PVT Analysis. *Polymers* **2018**, *10* (6), 578.

(30) Koptelov, A. A.; Karyazov, S. V. Effect of Pressure on the Thermal Decomposition of Polymers. *Dokl. Phys. Chem.* **2003**, *389*, 101.

(31) Bersted, B. H. Entanglement Network Model Relating Tensile Impact Strength and the Ductile-brittle Transition to Molecular Structure in Amorphous Polymers - Bersted - 1979. *J. Appl. Polym. Sci.* **1979**, *24* (1), 37–50.

(32) Hoy, R. S.; Foteinopoulou, K.; Kröger, M. Topological Analysis of Polymeric Melts: Chain Length Effects and Fast-Converging

Estimators for Entanglement Length. *Phys. Rev. E* **2009**, *80* (3), 031803.

(33) Kröger, M. Shortest Multiple Disconnected Path for the Analysis of Entanglements in Two- and Three-Dimensional Polymeric Systems. *Comput. Phys. Commun.* **2005**, *168* (3), 209–232.

(34) Shanbhag, S.; Kröger, M. Primitive Path Networks Generated by Annealing and Geometrical Methods: Insights into Differences. *Macromolecules* **2007**, *40* (8), 2897–2903.

(35) Tzoumanekas, C.; Theodorou, D. N. Topological Analysis of Linear Polymer Melts: A Statistical Approach. *Macromolecules* **2006**, *39* (13), 4592–4604.